applied sciences

MDPI

Article

A Study on Comparison of Temperature Distribution between Aluminum and GFRP Mold under Carbon Spar-Cap Manufacturing Process

Joong-Hoon Yoon [1], Jang-Ho Lee [2] and Sang-Il Lee [3,*]

[1] Department of Mechanical Engineering, Kunsan National University, Gunsan 54150, Korea; wndgns2987@gmail.com
[2] School of Mechanical System Engineering, Kunsan National University, Gunsan 54150, Korea; jangho@kunsan.ac.kr
[3] Institute of Offshore Wind Energy, Kunsan National University, Gunsan 54150, Korea
* Correspondence: silee@kunsan.ac.kr; Tel.: +82-63-469-8945; Fax: +82-63-469-7580

Abstract: In this study, temperature distribution as a function of the spar-cap thickness was numerically analyzed using a 20 kW wind carbon blade model. "Realizable k-ε", which was adopted as a turbulence model for heat transfer analysis, was effective in convection and diffusion calculations. SC/TETRA, a commercial thermal fluid analysis software, was used to calculate the heat flow from the heat panel to the outside boundary of the simulation model. In order to derive the equation for the temperature between the mold surface and the top surface of the spar-cap, the temperature interval of the heat panel was 10 °C, and the range was from 60 °C to 110 °C. As a result, the temperature distribution of the top surface of the spar-cap was insufficient to cure the Carbon Fiber Reinforced Plastic (CFRP) because the heat did not reach from the mold heat panel to the top surface of the carbon spar-cap. To resolve the problem of heat loss, the equation was derived by dividing the temperature boundary conditions between the mold surface and the spar-cap top surface as a function of the thickness of the carbon laminates. The temperature unevenness in the spar-cap curing process was reduced using the improved boundary condition. In addition, the cases where GFRP and aluminum were applied to the upper mold of the heat panel were compared using the same analysis method. An improvement to reduce the temperature non-uniformity of the spar-cap top surface was studied to solve the non-curing issue of the carbon spar-cap under the manufacturing process.

Keywords: spar-cap; heat transfer analysis; CFRP; thermal distribution; numerical analysis; wind turbine blade

Citation: Yoon, J.-H.; Lee, J.-H.; Lee, S.-I. A Study on Comparison of Temperature Distribution between Aluminum and GFRP Mold under Carbon Spar-Cap Manufacturing Process. *Appl. Sci.* **2022**, *12*, 5220. https://doi.org/10.3390/app12105220

Academic Editor: Wei Huang

Received: 1 April 2022
Accepted: 20 May 2022
Published: 21 May 2022

1. Introduction

The aerodynamic design of wind turbine blades plays an important role in determining the overall performance of the wind turbine. In order to increase the cross-sectional area through which the wind passes and to generate the maximum torque to drive the generator of a wind turbine, it is necessary to select a material with the appropriate weight and strength for the manufacture of large blades. Currently, most wind turbine blades are made of Fiber Reinforced Plastic (FRP), which can increase strength and efficiency to ensure lightness for design purposes [1,2]. Among the various FRPs, Glass Fiber Reinforced Plastic (GFRP), a composite material mainly used for wind turbine blades, is twice as strong in strength as steel of the same volume, and Carbon Fiber Reinforced Plastic (CFRP) is up to five times stronger in strength than steel. There is a study result that shows that the stiffness is twice as good, by up to eight times [3,4]. Although CFRP is superior to GFRP in many ways, it is relatively expensive, so it is common for blade manufacturers to mix the two materials to manufacture blades [5]. Wind turbine blades are manufactured using CFRP mainly for the spar-cap, which is the main structure of blades that requires high strength [6–10].

However, despite the fine mechanical properties of CFRP spar-caps, various defects that occur during the manufacturing process can cause blade failure. The spar-cap manufacturing process for wind turbine blades is mostly by hand, making defect prevention extremely difficult. Defects such as fiber misalignment [11] of the CFRP prepreg, the basic unit of the spar-cap, occur in the lamination process and make the spar-cap more brittle. As the content of this defect increases, fatigue resistance and corrosion resistance decrease, resulting in a significant decrease in shear strength and compressive strength [12,13]. In particular, various defects caused by voids due to uncured epoxy are considered to be the main causes of adverse effects on the physical characteristics of composite materials [14–16].

The content and size of defects that occur in the epoxy, the matrix constituting the CFRP of the spar-cap, are greatly affected by process conditions and the environment. From the viewpoint of heat transfer in terms of various environmental and process factors, uneven curing of the epoxy can cause residual stress formation in composite materials [17–19]. Residual stress in the epoxy is responsible for the formation of voids and various defects, which can cause catastrophic failure of the spar-cap.

In order to eliminate the temperature unevenness phenomenon of the curing process, it is necessary to specifically control the temperature of the spar-cap and use equipment such as an autoclave to maintain the same temperature at every position in the material. Due to the large size of wind turbine blades, the introduction of equipment is quite difficult with current technology [20]. Despite the fact that uneven curing is responsible for areas that have many effects on defect formation, heat transfer numerical analysis studies considering the thickness of the spar-cap are inadequate. Some blade manufacturers have made efforts to ensure the surface temperature unevenness of the spar-cap by installing a separate heat shield around the spar-cap mold to block a certain amount of heat loss, but the influence of the season is high. It is too large to alleviate the temperature unevenness phenomenon.

In fact, there was a report that measured the mold temperature during curing, recognizing the problem of spar-cap quality deterioration due to temperature. It became clear that the temperature of the mold was high in the thick part of the spar-cap. In this temperature measurement experiment, the uneven temperature due to the thickness was checked, and heat transfer numerical analysis research was required to solve this phenomenon.

Therefore, in order to improve the formability of the spar-cap, which is the most important structure in wind blades, heat transfer analysis research in the curing process is absolutely necessary. In this paper, a method was presented that can maintain the top-surface temperature of a spar-cap at a relatively constant level compared to the current method using heat transfer numerical analysis. In addition, the effects of aluminum, which is a mold used mainly for molding composite materials by infusion, and GFRP, which is a mold used for manufacturing spar-caps, on the spar-cap temperature distribution were compared.

2. Methodology

In this study, the correlation between the spar-cap top surface and the heat panel temperature was analyzed. In order to guide the spar-cap top surface to have even temperature distribution, reference models were introduced so that all conditions were the same except for the heat panel temperature. The reference model is used to understand the relationship between the spar-cap top surface temperature and the heat panel temperature. Applying the data obtained from the temperature measurement experiments of the spar-cap manufacture may ensure the accuracy of the numerical analysis, but this requires preparation for a fairly large experiment. A well-planned research facility is needed to ensure the accuracy of the experimental results. This chapter proves the temperature unevenness of the spar-cap rather than the strictness of the numerical value and proposes improvement measures. Since it is a step to confirm that it is applicable to the actual product, 6 reference models including heat conduction analysis were used. This reference model was used to transiently analyze the base temperature of the heat panel at 10 °C intervals from 60 °C to 110 °C for a total of 6 cases, as shown in Figure 1. For each reference model, it can be inferred that the surface temperature appears unevenly depending on the thickness and shape of the spar-cap. The obtained thermal formula can be obtained by mathematically calculating the relationship between the spar-cap top surface and the heat panel for each section of the model, a the temperature unevenness of spar-cap top-surface can be improved by changing the base temperature of the heat panel using the obtained thermal formula. Finally, in order to confirm the improvement of the temperature unevenness of the spar-cap top surface, a heat transfer simulation corresponding to Case 7 was performed and the temperature distribution was analyzed.

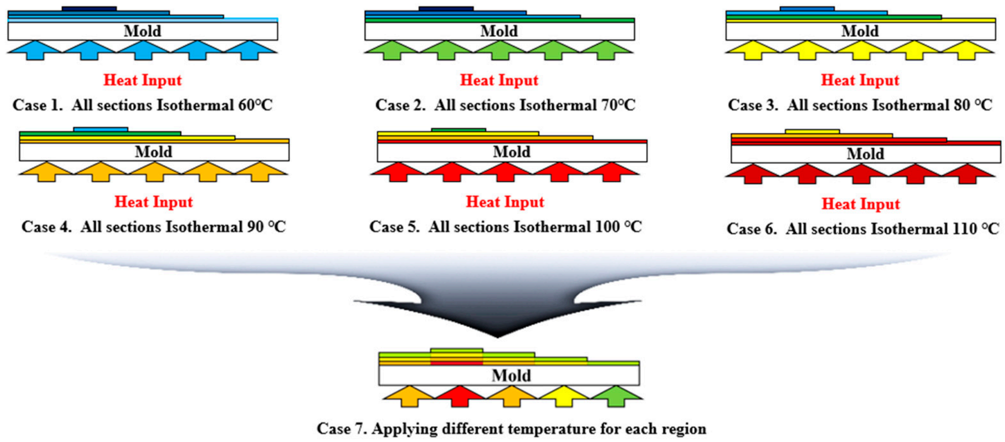

Figure 1. Method to improve temperature unevenness due to shape and thickness of spar-cap using reference models.

2.1. Geometrical Modeling

The geometry model in Figure 2a used in this study is a full-scale model of the 20 kW experimental wind turbine blade spar-cap and its mold in operation at Kunsan National University. The heat transfer simulation is analyzed by the transient method to confirm that the entire spar-cap manufacturing process has a time effect. With full-scale modeling, the need for computer resources is so great that a simplified model is used. In addition, thermal stress and deformation [21] due to the curvature of the spar-cap shape causes an increase in the surface area of the edges and more heat loss. This acts as an error in calculating the mean value of the spar-cap top face temperature distribution used in the obtained thermal formula. Therefore, to limit these problems, the full-scale spar-cap model, as shown in Figure 2a, chose a simplified model based on the center with the least heat loss due to edge effects. Therefore, spar-cap full-scale modeling went through a 3-D to 2.5-D simplification process. As shown in Figure 2b, the modeling of heat transfer analysis consists of five sections divided by the thickness step.

2.2. Mathematical Formulation

As shown in Figure 2b, the relational formula for the heat plate temperature and the spar-cap upper surface temperature for each section separated by the thickness offset was established. Figure 3 is a graph using $\overline{T}_{S,N}$, which is the average temperature of the spar-cap top surface of each section from case 1 to case 6, and $\overline{T}_{H,N}$, which is the average temperature of the heat panel. $\overline{T}_{S,N}$ and $\overline{T}_{H,N}$ are the average values for each section of the temperature distribution calculated by the heat transfer simulation. The obtained formula for each section shown in Figure 3 is a linear equation as with Equation (1). This equation can be used to determine the $T_{H,N}$ that can derive the desired spar-cap top face temperature for each section. B_N, which is a coefficient of $T_{M,N}$, and D_N, which is a constant, can be found in the process of establishing a trend equation.

$$T_{S,N} = B_N T_{H,N} + D_N \tag{1}$$

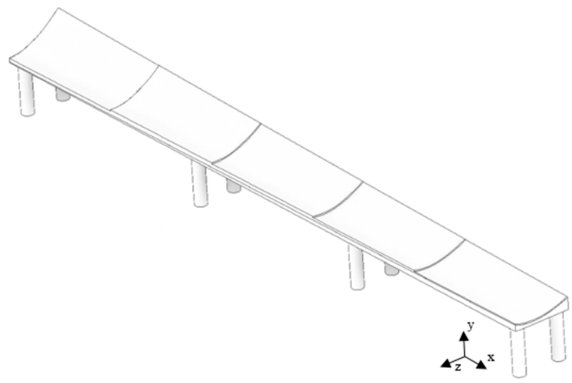

(a)

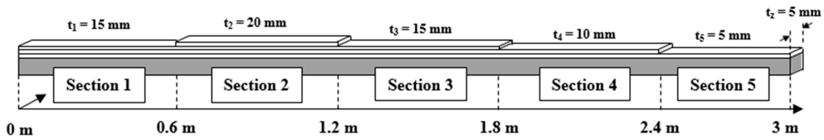

(b)

Figure 2. Spar-cap modeling for 20 kW wind turbine: (**a**) full-scale geometry model of heat transfer simulation; (**b**) schematic diagram of spar-cap modeling that defines dimensions and sections.

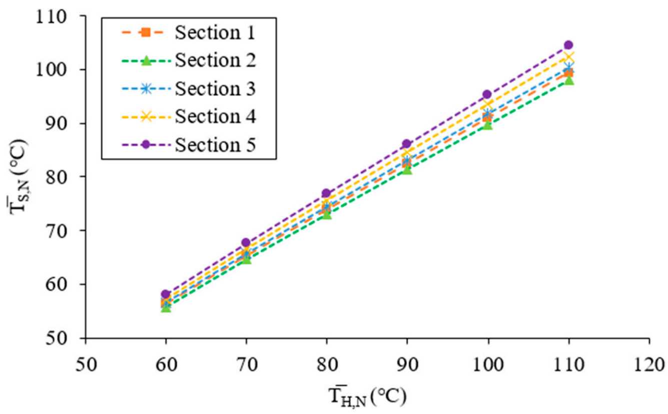

(a)

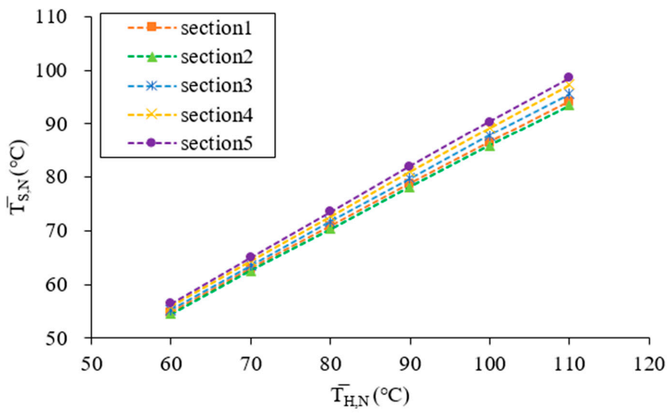

(b)

Figure 3. Obtained formula between heat panel temperature and top surface temperature of the spar-cap: (**a**) aluminum mold; (**b**) GFRP mold.

The governing equation for numerical analysis of heat transfer is a complex heat transfer consisting of heat conduction, convection, and radiation. The heat transfer simulation is performed by Equations (2)–(3) and (5)–(6). Equation (2) is a typical equation used to calculate the heat conduction inside the material. This calculates the heat conduction from the heat panel to the spar-cap top face. Thermal conductivity k, specific heat C, and density ρ are thermophysical properties of the material, and $\dot{e}_{gen}$ is the amount of heat generated from the heat panel. Assuming a heat panel is a volumeless surface, $\dot{e}_{gen}$ is defined as heat [W/m^2].

$$\nabla^2 T + \frac{\dot{e}_{gen}}{k} = \frac{k}{C\rho}\frac{\partial T}{\partial t} \tag{2}$$

Equation (3) can calculate the heat loss due to convection heat transfer on the spar-cap surface. For the heat transfer coefficient h, a method of calculating the total heat transfer coefficient of the spar-cap surface through a temperature measurement experiment may be common. However, calculating the heat transfer coefficient through experiments requires a large amount of equipment and human resources in a highly controlled environment. In addition, the size of the spar-cap is very large and there are many unpredictable environment variables, so h uses generalized values in natural convection conditions.

$$\dot{Q}_{conv} = hA_s\,(T_s - T_\infty) \tag{3}$$

Equation (4) serves to obtain the heat transfer coefficient h_r that determines the heat flux at the contact interface between the mold and the spar-cap. If the thickness and thermal conductivity of the epoxy coated on the contact interface are known, the heat transfer coefficient h_r of the contact interface can be obtained [22].

$$h_r = k_r\ /\ \delta \tag{4}$$

Radiation is often omitted in the process of simplifying the heat transfer simulation. However, in this model, the temperature difference between the spar-cap surface and the shielding film surface made of vinyl (which can conduct heat with the outside) is large, so the radiation is too large to ignore. Therefore, radiation calculates the mutual heat exchange between the spar-cap surface and the shield surface via Equation (5) called the view factor (VF) method. In Equation (5), the emissivity ε_1, ε_2, and temperature T_1, T_2 are the inherent characteristics of the object, then the calculation of radiation by distance and direction is performed. σ is a Stefan–Boltzmann constant, and $5.6703 \times 10^{-8}\ \left[\mathrm{W/m^2 \cdot K^4}\right]$ is a known value.

$$Q_{12} = \frac{A_1 F_{12}\varepsilon_1\varepsilon_2}{1 - F_{12}^2 \frac{A_1}{A_2}(1-\varepsilon_1)(1-\varepsilon_2)}\sigma\left(T_1^4 - T_2^4\right) \tag{5}$$

Among the turbulence models for flow analysis, the Realizable k-ε turbulence model [23] with excellent flow predictability of complex shapes was used to calculate the process in which heat emitted from the spar-cap surface diffuses through the air. In the Realizable k-ε turbulence model, the flow characteristics are determined by Equations (6)–(8). The lower the value of y +, the more stable this turbulence model can operate as compared with other turbulence models. The modeling grid used in this simulation has a very low y + of 10. The total number of grids used in the simulation was 2.6 million, and a tetra grid with a minimum unit length of about 1.6 mm was used. The tetra grid is one of the grids whose high quality in thermal fluid analysis has been verified. However, considering that the minimum thickness of the spar-cap is 5 mm, it is difficult to satisfy the rate of convergence because the grid having the smallest size is large. As a solution to this, several prism grids were introduced, prism grids are half the minimum unit length of the tetra grid, to improve the convergence.

$$\frac{\partial}{\partial t}(\rho\epsilon) + \frac{\partial}{\partial x_j}(\rho\epsilon u_j) = \frac{\partial}{\partial x_j}\left[\left(\mu + \frac{\mu_t}{\sigma_\epsilon}\right)\frac{\partial\epsilon}{\partial x_j}\right] + \rho C_1 S\epsilon - \frac{\rho C_2 \epsilon^2}{k + \sqrt{\nu\epsilon}} + C_{1\epsilon}\frac{\epsilon}{k}C_{3\epsilon}P_b + S_\epsilon \quad (6)$$

$$\eta = S\frac{k}{\epsilon} \quad (7)$$

$$S = \sqrt{2S_{ij}S_{ij}} \quad (8)$$

All models used in the heat transfer simulation were transiently analyzed because it was necessary to confirm the change in temperature distribution over time. Depending on the properties of the material or the environment, blade and spar-cap curing generally progresses slowly over a long period of time. The time at which the epoxy begins to cure during this process may vary depending on the location of the structure. Transient analysis is required to confirm the curing time and position due to this temperature unevenness. Transient analysis for heat transfer simulation was performed in 0.1 s per cycle to minimize the initial error of the analysis. From 1000 cycles when the values converged and entered the stabilization stage, analysis was performed for 100 s per cycle, and then the analysis phase time per cycle increased linearly. At 6 h of analysis when the simulation was completed, 450 s per cycle was calculated.

2.3. Material Properties and Boundary Conditions

In Chapter 2.1, modeling simplification for numerical analysis of heat transfer was described. This chapter defines the boundary conditions of the simplified model and the thermophysical properties of the solid, which is a heat transfer medium. The heat transfer mechanism of this numerical analysis model is as follows. The heat generated from the heat panel passes through the upper part of the mold and reaches the spar-cap interface. After that, the heat released from the mold is conducted to the spar-cap through a process of receiving thermal resistance due to contact between solids. The heat that has passed through the spar-cap is transferred from the spar-cap surface into the air, and convection heat transfer proceeds. The air warmed by convection transfers heat to the outside of the control volume. Along with this, irradiation is performed on the spar-cap surface, and finally heat is transferred to the outside of the control volume. The factor that determines the heat flux transferred from the solid to the fluid is the heat transfer coefficient h in Equation (3). Then, the method of realizing radiation is performed via the VF method of Equation (5). From the model's point of view, convection and radiation do not require complicated assumptions of boundary conditions and thermophysical properties for calculation. However, the spar-cap and its mold need to make some assumptions about thermophysical properties and boundary conditions.

In order to perform a heat transfer simulation, it is necessary to determine information about the boundary conditions and thermophysical property values of the target model. It is difficult to copy the actual heat transfer mechanism as it is for the boundary conditions and physical property values applied to the simulation. In particular, the method of simulating the composite material curing process causes problems to be considered from a microscopic point of view and problems to be considered from a macroscopic point of view. The schematic diagram in Figure 4 shows how to solve this problem by distinguishing between macroscopic and microscopic heat transfer.

Figure 4a, which is based on the y-z plane of Figure 2a, is a schematic cross-sectional view of the macroscopic heat transfer process. This figure shows how the heat generated by the heat panel is transferred to the spar-cap surface and is released out of the system by the action of radiation and convection heat transfer. This heat transfer system shows that there is no inflow of air and that the heat generated by the heat panel simply goes out as with convection or radiation. Since this method has limitations in achieving the microscopic structure of the composite and the boundary of the mold contact surface, a method was devised to implement the model as it is through several assumptions.

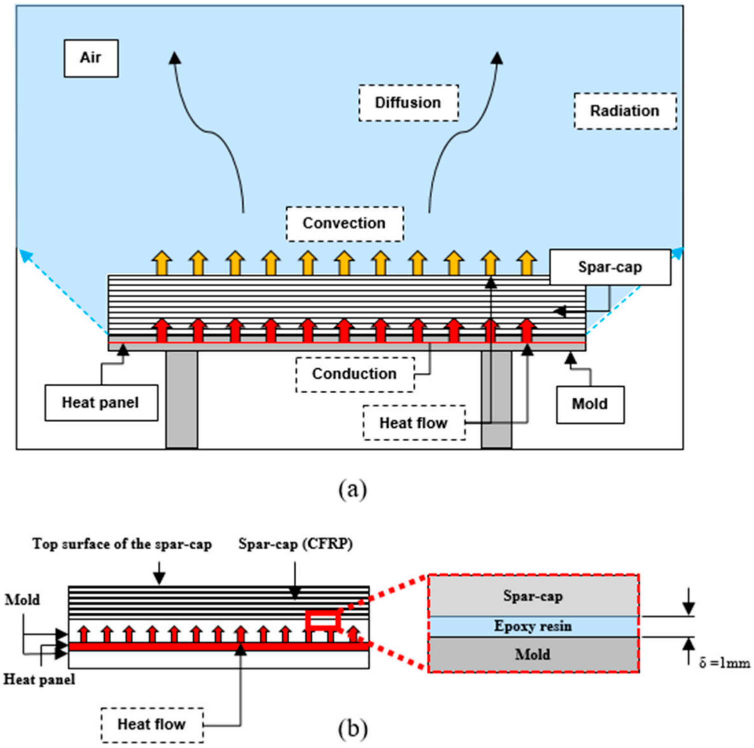

Figure 4. Cross-sectional view of boundary conditions for heat transfer simulation: (**a**) spar-cap manufacturing process; (**b**) contact heat conduction of the interface between spar-cap and mold.

First is the contact heat transfer between the mold and the spar-cap. When heat is transferred from the mold to the spar-cap, there is thermal resistance due to contact. The following assumptions were made in order to apply the contact interface h_r to the heat transfer simulation via Equation (4). Looking at Figure 4b, a thinly coated epoxy on the spar-cap bottom face is present at a constant thickness between the spar-cap and the mold. In order to obtain h_r that determines the heat flux on the contact surface between the mold and the spar-cap, the thermal conductivity k_r of the epoxy shown in Table 1 and an arbitrary thickness δ = 1 mm are substituted into Equation (4).

Table 1. Thermophysical properties of materials constituting CFRP.

Thermophysical Property	Value	
V_f	0.61	
ρ (kg/m^3)	ρ_f	1810
	ρ_r	1200
C (J/kg·K)	C_f	931 + 3.47 T
	C_r	750 + 2.05 T
k (W/m·K)	k_{f1}	2.4 + 5.07 × 10^{-3} T
	k_{f2}	7.69 + 1.56 × 10^{-2} T
	k_r	0.148 + 3.43 × 10^{-4} T

The second is a method of simplifying the microscopic fiber structure of a composite material and replacing it with one physical characteristic. The grid size of the FRP macro size model and the micro size model is very difficult to implement in one simulation because the scale difference is so large. However, the model used in this simulation has a minimum thickness of 5 mm and a maximum length of 3 m, so the macroscopic and microscopic properties of the composite must be implemented together. Therefore, the thermophysical properties of the fine fiber structure of the composite material have been simplified. CFRP, which is the main component of the spar-cap, has different thermophysical properties depending on the arrangement of fibers. If the fiber arrangement is unidirectional (UD), it can be simplified by using equations such as Equations (9)–(13) [24]. The GFRP mold also determined the thermophysical property values of the composite material mold by the microscopic method of simplifying the fiber structure of the CFRP spar-cap. Table 2 summarizes the thermophysical property values of isotropic materials and fluids used in the heat transfer simulation and the thermophysical property values of the CFRP obtained above. The values of aluminum and copper in Table 2 are constant numbers, which are thermophysical property values at room temperature provided by SC/Tetra. For the thermophysical properties of GFRP, the results of experiments conducted by Keller were applied [25,26]. The actual blade V_f (fiber volume fraction) of this study was used in Equations (9)–(13). Tables 1 and 2 summarize the results of simplifying thermophysical properties.

$$\rho = V_f \rho_f + \left(1 - V_f\right)\rho_r \tag{9}$$

$$C = V_f C_f + \left(1 - V_f\right) C_r \tag{10}$$

$$k_1 = V_f k_{1f} + \left(1 - V_f\right) k_r \tag{11}$$

$$k_2 = k_3 = k_r \left[\begin{array}{c} \left(1 - 2\sqrt{\frac{V_f}{\pi}}\right) \\ +\frac{1}{B}\left\{ \pi - \frac{4}{\sqrt{1 - \frac{B^2 V_f}{\pi}}} tan^{-1} \frac{\sqrt{1 - \frac{B^2 V_f}{\pi}}}{1 + B\sqrt{\frac{V_f}{\pi}}} \right\} \end{array} \right] \tag{12}$$

$$B = 2\left(\frac{k_r}{k_{2f}} - 1\right) \tag{13}$$

Table 2. Thermophysical properties of materials related to heat transfer analysis.

	Material	Density (kg/m^3)	Specific Heat (J/kg)	Conductivity (W/m)
Mold	Aluminum	2688.7	898.7	236.72
	GFRP	1870	1246.08	0.7166 * 0.4473 **
Spar-Cap	CFRP	1572.1	2.8651 T + 1636.5	0.0031 T + 2.2755 * 0.0011 T + 0.8052 **
Heat panel	Copper	8889.8	384.6	398.84

* The longitudinal direction. ** The transverse direction.

Thermal diffusion by convection uses air as a medium. The initial value of air and the standard temperature for certain physical properties is 30 °C, density $\rho_{air} = 1.164$ kg/m^3, thermal diffusion coefficient $\alpha_{air} = 0.00341$/K, viscosity coefficient $\mu_{air} = 1.83 \times 10^{-5}$ Pa·S, heat transfer coefficient $h_{air} = 10$ W/m^2·K, specific heat $C_{air} = 1007$ J/kg·K, thermal conductivity $k_{air} = 0.0256$ W/m·K.

2.4. Grid Independence Verification

The analysis model is selected by two methods, showing the numerical accuracy by the element quantity and the analysis time for the element quantity. An appropriate model was selected in consideration of analysis time and accuracy. Table 3 shows five models with different numbers of grids. Case 6 is a model that represents the number of grids used in this study. Case 6, which has the highest maximum temperature, requires more verification than other cases because the temperature deviation is large. Since the aluminum mold has more active heat transfer than the GFRP mold, case 6 using the aluminum mold is suitable as a grid independence verification model. All boundary conditions and physical properties were the same and only the number of grids was different to make cases A, B, C, and D. Case D is the most accurate grid model because it has the largest number of grids. Comparing the temperature difference between case D and the other cases, the accuracy of the model with a few number of grids is compared.

Table 3. The grid models for independence verification.

	Analysis Time (s)	Element Number
Case A	4184	70,925
Case B	13,006	271,010
Case C	61,401	353,936
Case 6	68,487	2,677,835
Case D	294,960	7,682,326

In Table 3, the spar-cap top surface temperatures at the same coordinates in each case were compared. In Figure 5a, in all cases except case A with the smallest number of grids, the spar-cap top surface temperature deviation for case D with the largest number of grids is less than 1 °C. This shows that verifying grid independence is a pointlessly small temperature deviation. The reason why temperature deviations below 1 °C are meaningless is that even temperature control in 1 °C increments is extremely difficult in actual manufacturing conditions. Since the control unit of a general temperature heating device is 1 °C, it is determined that all cases except case A are within the error range. Case D takes about 4 days to simulate, and it takes too long to simulate all cases depending on the mold type and heat panel temperature. On the other hand, Case 6 requires an acceptable analysis time of about one day. Therefore, in consideration of the analysis time, Case 6, having fewer grids than Case D, was selected as the grid model of this study.

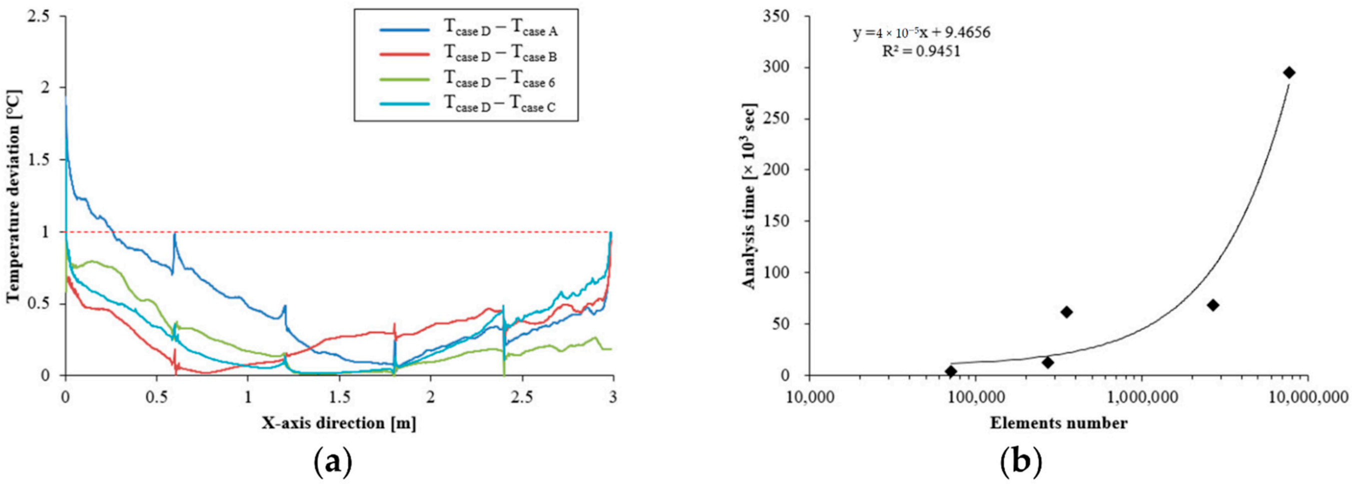

Figure 5. Methods for selecting the suitable grid model: (**a**) temperature deviations of other grid models with respect to Case D as the good quality grid model; (**b**) analysis time according to the number of grids.

2.5. Methodology for Establishing Obtained Formulas

The obtained formula establishment method for improving the temperature unevenness phenomenon of spar-cap was devised as follows. The obtained formula such as Equation (1) can obtain the temperature $T_{H,N}$ of the heat panel that alleviates the temperature unevenness based on the steady state analysis. To find $T_{H,N}$, use $\overline{T}_{S,N}$ and $\overline{T}_{H,N}$. $\overline{T}_{S,N}$

and $\overline{T}_{H,N}$ are the average temperature distributions for each section obtained by the heat transfer simulation of the reference model. For example, the $\overline{T}_{S,N}$ of section 1 for which the heat transfer simulation was completed using the aluminum mold is 56.35 °C, 65.28 °C, 73.88 °C, 82.42 °C, 90.91 °C, 99.33 °C from case 1 to 6, respectively. The corresponding $\overline{T}_{H,N}$ is 60 °C, 70 °C, 80 °C, 90 °C, 100 °C, 110 °C from case 1 to 6, respectively. Looking at Figure 3a, the temperature of section 1 corresponds to $\overline{T}_{S,N}$ and $\overline{T}_{H,N}$ in terms of points. Then, if a liner equation is created with $\overline{T}_{H,N}$ on the horizontal axis and $\overline{T}_{S,N}$ on the vertical axis, it is calculated as $T_{S,1}$ = 0.8582 $T_{M,1}$ + 5.0841. Substituting the optimum curing temperature of 80 °C for $T_{S,1}$, $T_{H,N}$ is calculated as 87.2942 °C. Calculations were made in the same way, and the trend models for each section are summarized in Table 4.

Table 4. Heat panel temperature by section to which obtained formula is applied.

Mold	Section Number	Obtained Formula	Target Temperature of Spar-Cap Top Surface ($T_{S,N}$)	Improved Heat Panel Temperature ($T_{H,N}$)
Aluminum	1	$T_{S,1} = 0.8582\ T_{M,1} + 5.0841$	80 °C	87.2942 °C
	2	$T_{S,2} = 0.8435\ T_{M,2} + 5.4083$	80 °C	88.4312 °C
	3	$T_{S,3} = 0.8733\ T_{M,3} + 4.4058$	80 °C	86.5615 °C
	4	$T_{S,4} = 0.8999\ T_{M,4} + 3.5054$	80 °C	85.0034 °C
	5	$T_{S,5} = 0.9262\ T_{M,5} + 2.6795$	80 °C	83.4814 °C
GFRP	1	$T_{S,1} = 0.7859\ T_{M,1} + 7.8966$	80 °C	91.7463 °C
	2	$T_{S,2} = 0.7779\ T_{M,2} + 7.9987$	80 °C	92.5586 °C
	3	$T_{S,3} = 0.8063\ T_{M,3} + 7.0694$	80 °C	90.4510 °C
	4	$T_{S,4} = 0.8270\ T_{M,4} + 6.4472$	80 °C	88.9393 °C
	5	$T_{S,5} = 0.8434\ T_{M,5} + 5.9729$	80 °C	87.7722 °C

3. Results

3.1. Reference Model's Spar-Cap Top Face Temperature Results of Steady State Analysis

Figure 6a, which is the aluminum mold of the reference model, and Figure 6b, which is the GFRP mold of the reference model, are the steady state temperature distributions of the spar-cap top face. Figure 6a,b show that the temperatures are clearly discontinuous at some point in the spar-cap thickness offset. Furthermore, case 6, having the highest base temperature of the heat panel, showed a phenomenon that the temperature deviation of the discontinuity point was relatively large as compared with the other cases. The cause of this phenomenon can be understood by comparing the turbulence dissipation rate and the average flow velocity of case 1 and case 6 where the base temperature difference of the heat panel is maximum. Random points were selected in the spar-cap model convection region. The turbulence dissipation rate and flow velocity of these points were averaged to calculate the turbulence dissipation rate of the system. In the case of the model using the GFRP mold, case 6 has a 3.6 times higher turbulence dissipation rate and 1.8 times higher average flow velocity than case 1. It can be seen that the higher the temperature of the heat source, the more active the heat diffusion and convection is, and the larger the heat loss rate on the spar-cap surface. Since the higher the temperature of the heat source is the larger the heat loss on the surface, it can be seen that the temperature change in the thick section of the spar-cap is large.

3.2. Case 7 Model's Spar-Cap Top Surface Temperature Results of Steady State Analysis

Figure 7 shows the spar-cap top surface temperature of Case 7 to which $T_{\mathrm{H,N}}$ in Table 4 is applied to compare with the top surface temperature of the reference model. Looking at Case 7 in Figure 7, the spar-cap surface temperature tends to maintain an average of 80 °C regardless of the type of mold. However, a similar temperature discontinuity still existed at the offset position in Figure 6 of the reference models.

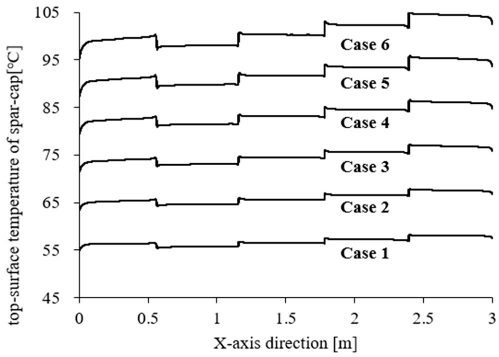

(a)

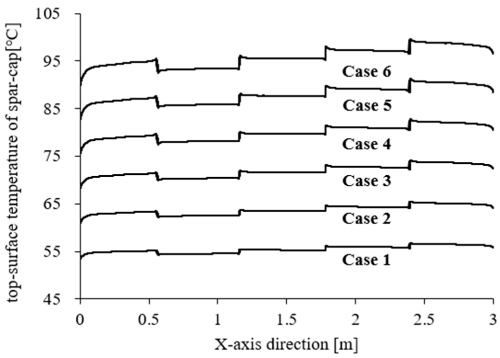

(b)

Figure 6. Top-surface temperature of spar-cap with steady state analysis (reference models): (**a**) aluminum mold; (**b**) GFRP mold.

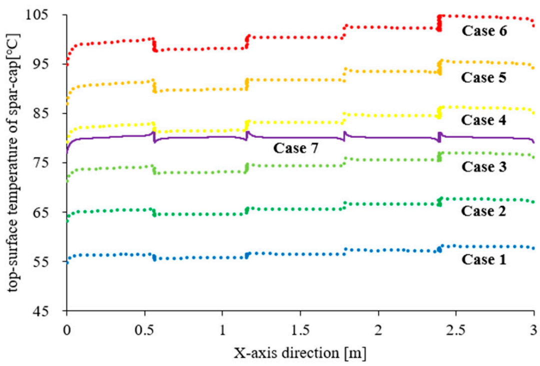

(a)

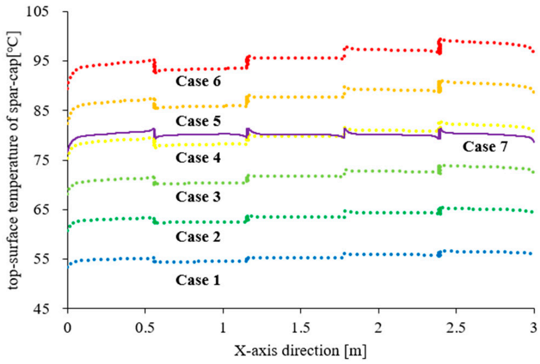

(b)

Figure 7. Top-surface temperature of spar-cap comparison between improvement model and the reference model on steady state analysis: (**a**) aluminum mold; (**b**) GFRP mold.

3.3. Comparison of Steady State Analysis Temperature Distributions between Contact Interfaces of Materials

It was confirmed that the graph shapes of Case 7 in Figure 7a and Case 7 in Figure 7b are slightly different. In order to recognize the cause of the difference in the graph shape, the temperature distributions of the spar-cap top surface, mold top surface, and heat panel were compared as shown in Figure 8. This figure clearly shows the cause of the slight temperature distribution difference between the aluminum mold and the GFRP mold. For aluminum molds, the temperature of the mold top surface tends to be approximately the same as the temperature of the heat panel. Since the aluminum mold has high thermal conductivity, it can be seen that the spar-cap top surface temperature response delay when changing the base temperature of the heat panel is relatively short compared to the GFRP mold. On the other hand, Figure 8b shows that the top surface temperature of the GFRP mold has a non-linear temperature distribution between the spar-cap top surface and the heat panel. Therefore, as the temperature of the heat panel becomes higher, the spar-cap top surface temperature can be kept even.

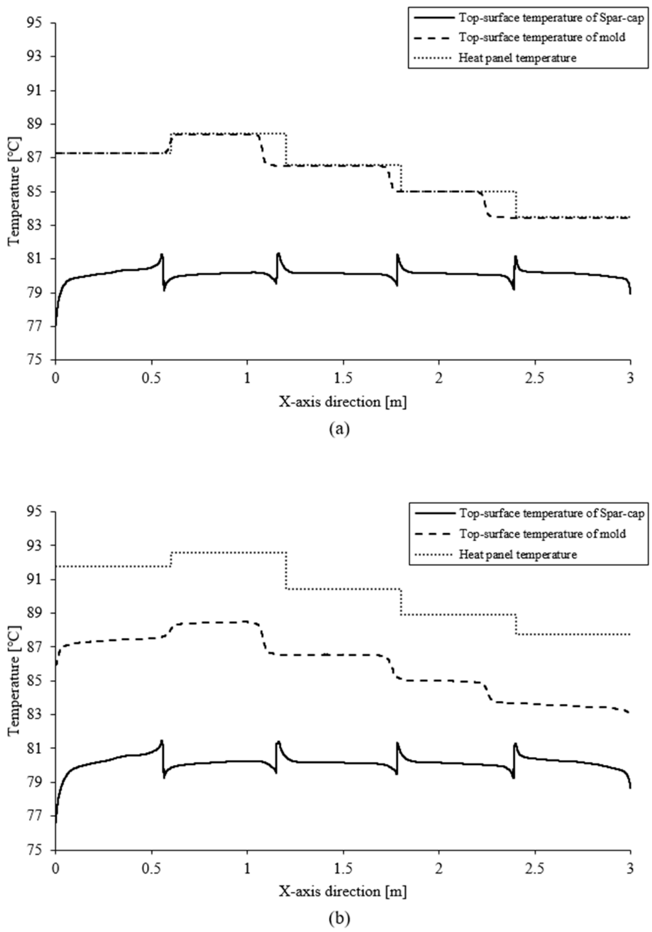

Figure 8. Temperature comparison among mold top surface, spar-cap top surface and heat panel: (**a**) aluminum mold; (**b**) GFRP mold.

3.4. Spar-Cap Top Surface Temperature Results of Transient State Analysis

If the top surface has an uneven temperature distribution in the spar-cap manufacturing process, the time to reach the glass transition temperature is also uneven. If the time to reach the glass transition temperature is not even in one solid, various defects can occur. Figures 9 and 10 show some results of transient analysis to observe the change in the temperature distribution of the spar-cap top-surface over time.

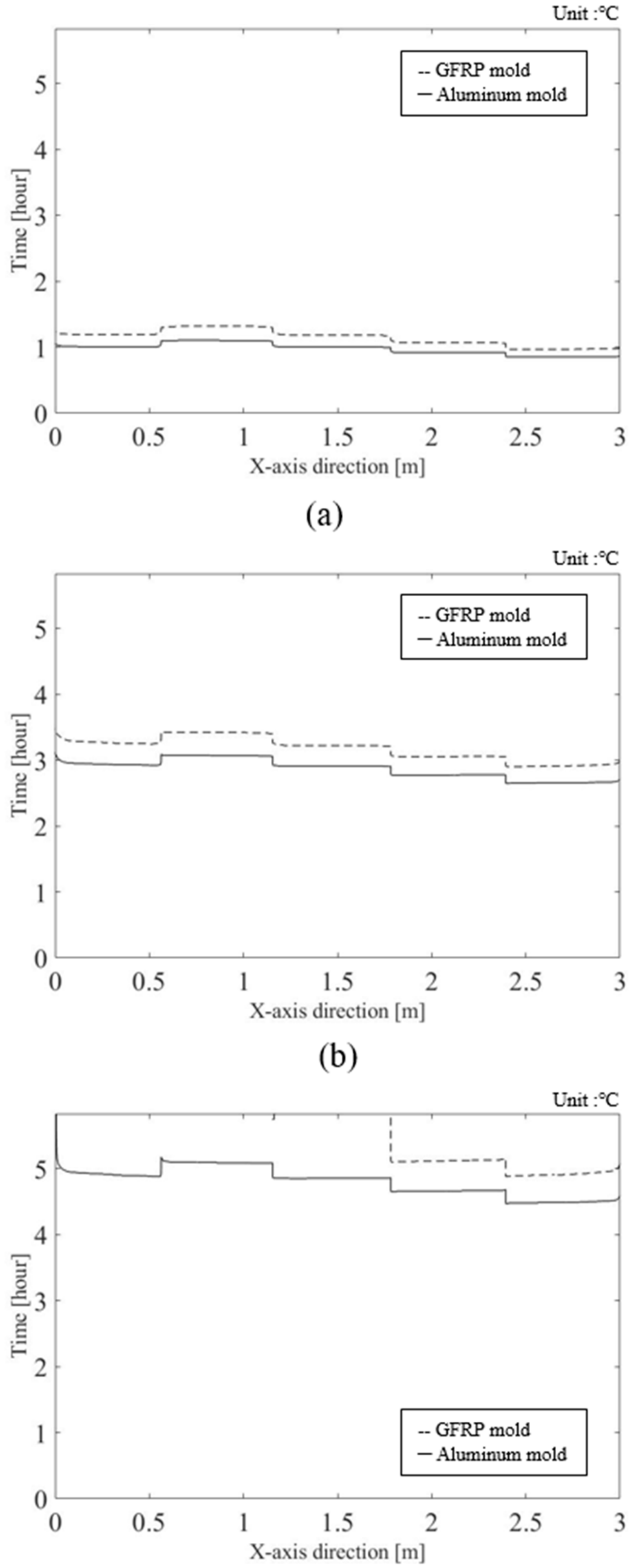

Figure 9. Top surface temperature of spar-cap on transient state analysis (case 4 at reference models): (**a**) 40 °C; (**b**) 60 °C; (**c**) 80 °C.

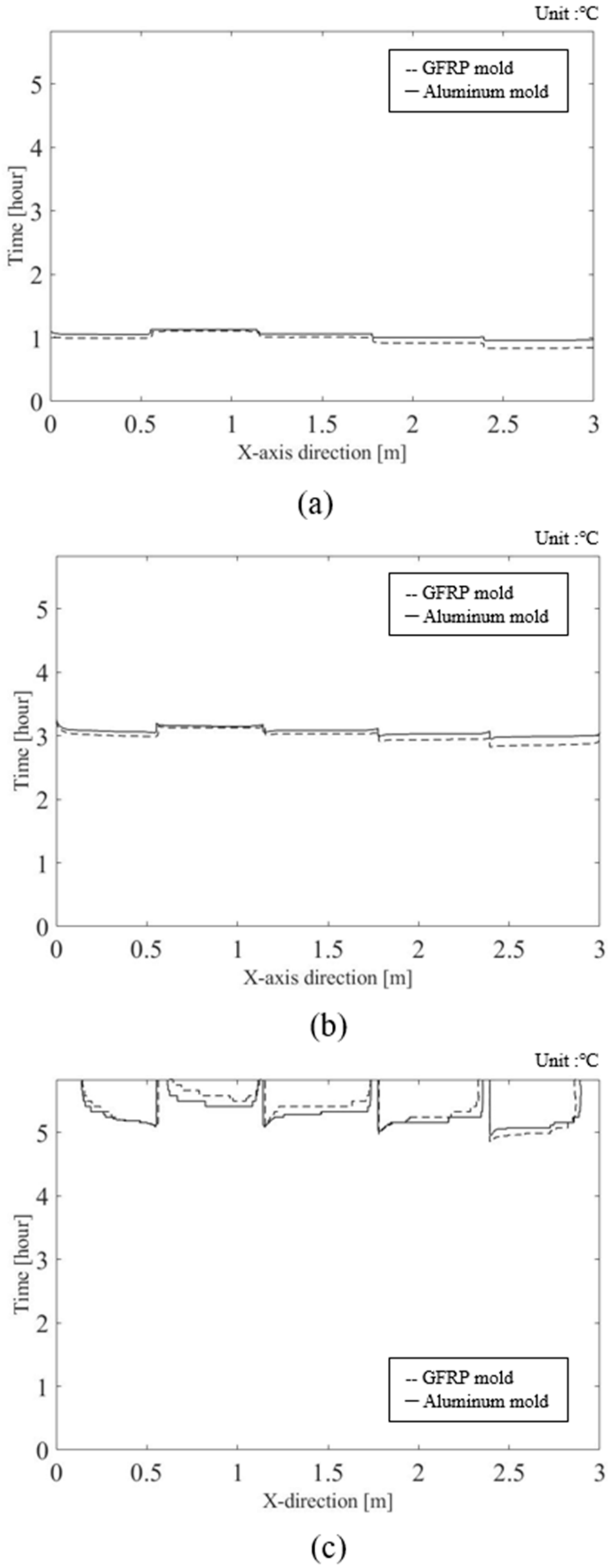

Figure 10. Top surface temperature of spar-cap on transient state analysis (case 7 at reference models): (**a**) 40 °C; (**b**) 60 °C; (**c**) 80 °C.

Figure 9 shows that the heating rate of the spar-cap top surface differs depending on the type of mold. Additionally, the higher the temperature over time, the greater the temperature difference between the sections of the spar-cap. As shown in Figure 9c, assuming a curing temperature of 80 °C, the epoxy curing of section 5 begins first at about 4 h 30 min after the heating is started, and the epoxy curing of section 2 starts at the latest after 5 h 10 min. In other words, the entire spar-cap takes about 40 min to cure. It can be seen that when the GFRP mold is used, all regions except sections 4 and 5 are not satisfied with the curing temperature conditions.

In Figure 10, in which the heating temperature was improved, a large difference in heating rate between the molds was not observed as compared with Figure 9. Over time, the temperature difference between the sections of the spar-cap also decreases. As shown in Figure 10c, curing progresses at similar times in all spar-cap sections.

In summary, it can be determined that the reference model (cases 1 to 6) is vulnerable to thermal stress and deformation because the cured zone and the uncured zone coexist in one spar-cap over 40 min. On the other hand, in Case 7, since the coexistence time of the cured zone and the uncured part is relatively short, 10 to 20 min, it can be determined that the curing process has been improved.

4. Conclusions

Methods to improve the curing process have been studied to minimize spar-cap defects that can damage wind blades. The same temperature was applied all at once under the spar-cap whose thickness was not continuous, and the existing manufacturing process method in which the temperature on the surface of the spar-cap was uneven was realized by heat transfer simulation. Then, in order to give optimized curing conditions for the spar-cap, an obtained formula with different thicknesses of the spar-cap model was introduced to analyze the heat transfer characteristics of the modeling. As a result, it was confirmed that the spar-cap surface temperature was improved in the steady state, and that there was a slight temperature improvement effect in the transient state. In the transient state, the model before improvement had the epoxy phase overlapped for 40 min, but the model after improvement proceeded to cure for 20 min. In future research, it seems necessary to proceed with research to give a different temperature rise rate for each section in the spar-cap curing process so that the temperature will be even in the process of temperature rise.

Author Contributions: Conceptualization, S.-I.L.; Formal analysis, J.-H.Y. and S.-I.L.; Investigation, J.-H.Y.; Methodology, J.-H.Y. and J.-H.L.; Software, J.-H.Y. and J.-H.L.; Writing—original draft, J.-H.Y.; Writing—review & editing, S.-I.L. All authors have read and agreed to the published version of the manuscript.

Funding: This work was supported by the Technology Innovation Program (20011732, Commercial development of carbon pultrusion materials and rotor blade for 3MW large scale wind turbine) funded By the Ministry of Trade, Industry & Energy (MOTIE, Korea).

Institutional Review Board Statement: Not applicable.

Informed Consent Statement: Not applicable.

Data Availability Statement: The data used in this study is available on requests from the corresponding author.

Conflicts of Interest: The authors declare no conflict of interest.

Nomenclature

A_1,A_2	Area (view factor method)	[m^2]
A_S	Spar-cap surface area	[m^2]
B_N	Gradient of the obtained formula	
C	Specific heat	[J/kg °C]
C_{air}	Air specific heat	
D_N	Constant of the obtained formula	
$\dot{e}_{gen}$	Surface heat generation	[W/m^2]

F_{12}	View factor (view factor method)	
h	Heat transfer coefficient	[W/m^2 °C]
h_{air}	Heat transfer coefficient of air	[W/m^2·K]
k	Thermal conductivity	[W/m °C]
k_{air}	Air thermal conductivity	[W/m °C]
k_r	Resin thermal conductivity	[W/m °C]
N	Section in the geometrical model	
$\dot{Q}_{conv}$	Convection heat transfer	[W/m^2]
T_S	Local spar-cap top surface mean temperature	
T_∞	Air temperature	
$\overline{T}_{S,N}$	Spar-cap top surface mean temperature	
$\overline{T}_{H,N}$	Heat panel mean temperature	[°C]
$T_{S,N}$	Desired spar-cap top surface temperature	[°C]
$T_{H,N}$	Improved temperature of the heat panel	
t_N	Thickness of spar-cap section	
t_Z	Z direction thickness of simplified model	[mm]
α_{air}	Air thermal diffusion coefficient	[1/K]
δ	Thickness of the epoxy coated on the spar-cap surface	[mm]
ε_1,ε_2	Emissivity (view factor method)	
σ	Stefan–Boltzmann constant	[W/m^2 ·K^4]
μ	Viscosity coefficient	[Pa·S]
μ_{air}	Air viscosity coefficient	[Pa·S]
ρ	Density	[kg/m^3]

References

1. Cox, K.; Echtermeyer, A. Structural Design and Analysis of a 10MW Wind Turbine Blade. *Energy Procedia* **2012**, *24*, 194–201. [CrossRef]
2. Beukers, A.; van Hinte, E. *Designing Lightness*; NAI010 Publishers: Rotterdam, The Netherlands, 2020.
3. Naser, M.Z.; Hawileh, R.A.; Abdalla, J.A. Fiber-reinforced polymer composites in strengthening reinforced concrete structures: A critical review. *Eng. Struct.* **2019**, *198*, 109542. [CrossRef]
4. Carbon Fiber vs. Fiberglass: A Comparison between the Two Materials Which Material Is Superior? 2017. Available online: https://infogr.am/carbon-fiber-vs-fiberglass (accessed on 13 January 2022).
5. Lee, E.B.; Lee, K.C.; Naughton, B.T.; Norris, R.E.; Sujit, D.; Lee, D.; Miller, D. *Optimized Carbon Fiber Composites in Wind Turbine Blade Design*; Sandia Report, SAND2019-14173; Sandia National Lab.: Albuquerque, NM, USA, 2019.
6. Brøndsted, P.; Nijssen, R. (Eds.) *Advances in Wind Turbine Blade Design and Materials*; Woodhead Publishing: Oxford, UK, 2013.
7. Thomsen, O.T. Sandwich Materials for Wind Turbine Blades—Present and Future. *J. Sandw. Struct. Mater.* **2009**, *11*, 7–26. [CrossRef]
8. Mishnaevsky, L.; Branner, K.; Petersen, H.N.; Beauson, J.; McGugan, M.; Sørensen, B.F. Materials for Wind Turbine Blades: An Overview. *Materials* **2017**, *10*, 1285. [CrossRef] [PubMed]
9. Grande, J.A. Wind Power Blades Energize Composites Manufacturing. *Plast. Technol.* **2008**, *54*, 68–75.
10. Khan, Z.I.; Arsad, A.; Mohamad, Z.; Habib, U.; Zaini, M.A.A. Comparative study on the enhancement of thermo-mechanical properties of carbon fiber and glass fiber reinforced epoxy composites. *Mater. Today Proc.* **2020**, *39*, 956–958. [CrossRef]
11. Vogler, T.; Kyriakides, S. On the initiation and growth of kink bands in fiber composites: Part I. experiments. *Int. J. Solids Struct.* **2001**, *38*, 2639–2651. [CrossRef]
12. Hernández, S.; Sket, F.; González, C.; Llorca, J. Optimization of curing cycle in carbon fiber-reinforced laminates: Void distribution and mechanical properties. *Compos. Sci. Technol.* **2013**, *85*, 73–82. [CrossRef]
13. Liebig, W.; Leopold, C.; Schulte, K. Photoelastic study of stresses in the vicinity of a unique void in a fibre-reinforced model composite under compression. *Compos. Sci. Technol.* **2013**, *84*, 72–77. [CrossRef]
14. Hapke, J.; Gehrig, F.; Huber, N.; Schulte, K.; Lilleodden, E. Compressive failure of UD-CFRP containing void defects: In situ SEM microanalysis. *Compos. Sci. Technol.* **2011**, *71*, 1242–1249. [CrossRef]
15. Olivier, P.; Cottu, J.; Ferret, B. Effects of cure cycle pressure and voids on some mechanical properties of carbon/epoxy laminates. *Composites* **1995**, *26*, 509–515. [CrossRef]
16. Huang, H.; Talreja, R. Effects of void geometry on elastic properties of unidirectional fiber reinforced composites. Compos. *Sci. Technol.* **2005**, *65*, 1964–1981.
17. Lange, J.; Toll, S.; Manson, J.-A.E.; Hult, A. Residual stress build-up in thermoset films cured above their ultimate glass transition temperature. *Polymer* **1995**, *36*, 3135–3141. [CrossRef]

18. Wineman, A.; Heinrich, C.; Nguyen, N.; Waas, A. A general network theory for the development of curing stresses in an epoxy/fiber composite. *Acta Mech.* **2016**, *227*, 3585–3601. [CrossRef]
19. Umarfarooq, M.A.; Gouda, P.S.; Banapurmath, N.R.; Edacherian, A. Impact of Process Induced Residual Stresses on Interlaminar Fracture Toughness in Carbon Epoxy Composites. *Compos. Part A Appl. Sci. Manuf.* **2019**, *127*, 105652. [CrossRef]
20. Marsh, G. 'De-autoclaving' prepreg processing. *Reinf. Plast.* **2012**, *56*, 20–25. [CrossRef]
21. Hsiao, K.-T.; Gangireddy, S. Investigation on the spring-in phenomenon of carbon nanofiber-glass fiber/polyester composites manufactured with vacuum assisted resin transfer molding. Compos. *Part A Appl. Sci. Manuf.* **2008**, *39*, 834–842. [CrossRef]
22. Madhusudana, C.V. *Thermal Contact Conductance*; Mechanical Engineering Series; Springer International Publishing: Cham, Switzerland, 2014.
23. Davis, P.L.; Rinehimer, A.T.; Uddin, M. A comparison of RANS-based turbulence modeling for flow over a wall-mounted square cylinder. In Proceedings of the 20th Annual Conference of the CFD Society of Canada, Canmore, AB, Canada, 9–11 May 2012.
24. Li, X.; Wang, J.; Li, S.; Ding, A. Cure-induced temperature gradient in laminated composite plate: Numerical simulation and experimental measurement. *Compos. Struct.* **2020**, *253*, 112822. [CrossRef]
25. Keller, T.; Zhou, A.; Tracy, C.; Hugi, E.; Schnewlin, P. Experimental study on the concept of liquid cooling for improving fire resistance of FRP structures for construction. *Compos. Part A Appl. Sci. Manuf.* **2005**, *36*, 1569–1580. [CrossRef]
26. Keller, T.; Tracy, C.; Huge, E. Fire endurance of loaded and liquid-cooled GFRPslabs for construction. *Compos. A Appl. Sci. Manufact.* **2006**, *37*, 1055–1067. [CrossRef]